https://doi.org/10.5194/egusphere-2026-1
Preprint. Discussion started: 11 February 2026

Assessing the reliability of firn microstructural measurements from micro-CT data

Kaitlin Keegan[1], Sarah Day[2], Yu-Min Chung[3], and Michael Gardner[4]

[1]Nevada Geosciences, Department of Geological Sciences and Engineering, University of Nevada Reno, Reno, NV
[2]Mathematics, William & Mary, Williamsburg, VA
[3]Eli Lilly and Company, Indianapolis, IN 46225, USA
[4]Civil and Environmental Engineering, University of California Davis, Davis, CA

Correspondence: K. Keegan (kkeegan@unr.edu)

Abstract. X-ray micro-computed tomography (micro-CT) has become a common technique used to characterize the microstructure of snow and firn, yet the sensitivity of micro-CT-derived microstructural parameters to image processing choices remains poorly understood. In particular, the selection of a binarization threshold can influence the reconstructed representation of the microstructure and, thus, any quantitative properties computed from it. Here, we systematically evaluate the sensitivity of six firn microstructural parameters to binarization threshold choice using micro-CT data from three samples of the NEEM 2009 S2 firn core that were extracted from shallow (7 m), intermediate (26 m), and deep (70 m) depths of the core. We generated reconstructions of the microstructure of each sample at every threshold value across the grayscale threshold range, and compare three thresholding approaches representing subjective, statistical, and topological strategies. Microstructural parameters describing bulk volume-fraction properties (Percent Object Volume, Percent Open Porosity, and Surface Area to Volume ratio) and microstructural complexity (Structural Model Index, Surface Convexity, and Euler Number) were computed across the full grayscale threshold range and evaluated using a normalized sensitivity metric. We find that bulk volume-fraction parameters are robust to threshold choice across all firn depths, while parameters describing microstructural complexity and connectivity exhibit strong threshold and depth-dependent sensitivity. Modeled estimates of the intrinsic permeability of the reconstructed microstructures generated at threshold values between 60-120 for each sample underscore the impact of threshold choice on the microstructural complexity and connectivity. These results demonstrate that binarization threshold choice can substantially influence interpretations of firn microstructural complexity and, therefore, transport properties, highlighting the need for careful selection of image processing steps, including binarization, in firn micro-CT studies.

1 Introduction

In polar regions, glaciers and ice sheets form through the continual accumulation of snow under persistently cold conditions. As this snow is buried, compacted, and aged without melting, it becomes *firn*, an intermediate material between snow and glacial ice. The firn column (Fig. 1a) consists of layers of partially compacted snow with interconnected pore space that progressively densifies until it reaches the density (ρ) of glacial ice (~$830 kg/m^3$; Cuffey and Paterson (2010)). Accurate knowledge of firn depth and its internal structure is essential for a range of glaciological applications, including the interpretation of ice-core

https://doi.org/10.5194/egusphere-2026-1
Preprint. Discussion started: 11 February 2026

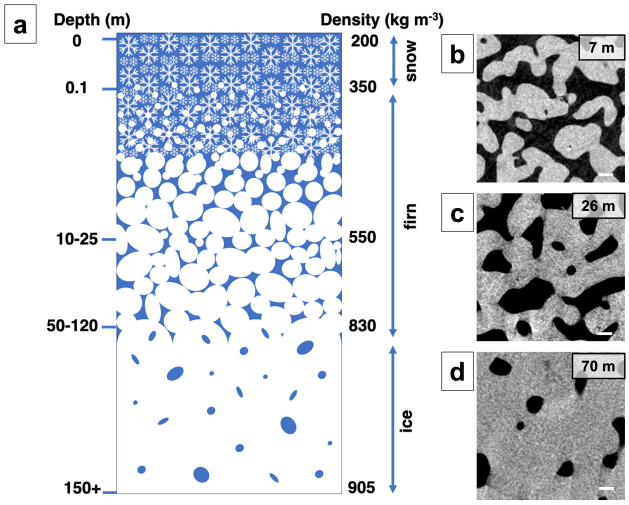

Figure 1. (a) A firn column schematic where white and blue regions represent the ice and pore space within the firn, respectively (Keegan (2022)). (b-d) A grayscale 2-D slice of the (b) 7 m, (c) 26 m, and (d) 70 m samples, derived from micro-CT data. In the grayscale images, gray pixels represent ice and black pixels represent pore space.

paleoclimate records, estimation of ice mass-balance from satellite altimetry data, and the assessment of firn's capacity to store meltwater (Schwander and Stauffer (1984); Helsen et al. (2008); Forster et al. (2014); FirnSymposiumTeam (2024)). With increasing depth in the firn column, layers not only become denser, but their microstructure also evolves. Characterizing this microstructural evolution is critical for improving our understanding of firn compaction physics and refining models used to estimate firn properties (Lundin et al. (2017)).

Over the past two decades, X-ray micro-computed tomography (micro-CT) has emerged as a powerful, non-destructive tool for imaging firn microstructure (Coléou et al. (2001); Lundy et al. (2002); Freitag et al. (2004); Heggli et al. (2011); Lomonaco et al. (2011)). Compared with traditional thin-section techniques, micro-CT enables the acquisition of two-dimensional (2-D) and three-dimensional (3-D) microstructural data substantially more rapidly and at higher resolutions (Gow (1969)). During micro-CT scanning, a sample is imaged as a series of 2-D grayscale images, or 'slices' (Fig. 1b-d), which can be reconstructed to form a 3-D representation of the original sample microstructure. Together, these 2-D and 3-D datasets provide detailed, high-resolution information on firn microstructure.

To analyze and quantify firn microstructure from micro-CT data, the grayscale images must be post-processed. This post-processing typically includes selecting a binarization threshold to convert grayscale images into binarized representations, as well as applying image "cleaning" procedures to remove artifacts introduced during measurement and binarization, among others. The choices made at each of these steps directly influence the resulting representation of the microstructure and, consequently, any quantitative metrics computed from it. Previous studies have highlighted the impact of image processing steps

https://doi.org/10.5194/egusphere-2026-1
Preprint. Discussion started: 11 February 2026

when analyzing micro-CT data of porous media (Kaestner et al., 2008; Iassonov et al., 2009), including the computation of the Specific Surface Area (SSA) of snow and near-surface firn (Flin et al., 2011; Hagenmuller et al., 2013, 2016). However, at present, no universal or standardized post-processing methodology exists for firn micro-CT datasets.

Often, the first image-processing step is the selection of a binarization threshold to convert grayscale images into binary (black-and-white) representations. This process assigns a value of 1 (white) to all image pixels with a grayscale intensity greater than and equal to, and 0 (black) to pixels with an intensity less than, the threshold value. Numerous strategies for determining this threshold have been developed, including Otsu's Method, the Persistence Diagram (PD) threshold method, and graphical user interfaces within instrument software to visually select a threshold (Otsu (1975); Chung and Day (2018)). The sensitivity of reconstructed microstructural parameters, beyond density and SSA, to binarization threshold choice has yet to be evaluated. This lack of standardization complicates comparisons across studies and introduces uncertainty into firn property estimates derived from micro-CT data. In this study, we examine how the choice of binarization threshold, a consequential post-processing step, affects the reconstructed firn microstructure and the measurements computed from it.

2 Methods

2.1 Firn Samples

For this study, we utilize micro-CT images of three firn core sub-samples (approximately $10 \times 10 \times 15\ mm$) obtained from the NEEM 2009 S2 firn core drilled in 2009 at the North Greenland Eemian Ice Drilling (NEEM) site (Keegan et al. (2014); NEEMCommunityMembers (2013)). The samples were extracted from distinct, homogeneous firn layers at depths of 7, 26, and 70 m, representing shallow ($\rho < 550\ kg/m^3$), intermediate ($550\ kg/m^3 < \rho < 730\ kg/m^3$), and deep ($\rho > 730\ kg/m^3$) zones of the NEEM firn column, respectively (Hörhold et al. (2011)). The 'parent' firn core pieces from which the samples were taken were approximately $100\ mm$ long and $81\ mm$ in diameter, with measured densities of 450, 620, and $810\ kg/m^3$ at 7, 26, and 70 m depth, respectively (Keegan et al. (2019); Keegan (2018)).

Each sub-sample was cut from its parent core section using a bandsaw housed in a cold laboratory maintained at $-10\,^{\circ}\mathrm{C}$, and subsequently stored at approximately $-18\,^{\circ}\mathrm{C}$ until imaging. Samples were oriented to preserve the original vertical (depth) direction of the core and were visually inspected prior to imaging to avoid fractures or handling-induced damage.

2.2 Micro-CT

2.2.1 System and Settings

The firn samples were imaged using a SkyScan 1172 micro-CT system adapted for operation in a cold laboratory that was maintained at $-10\,^{\circ}\mathrm{C}$ (Fig. 2). The samples were imaged in their frozen state, and each scan was conducted with an X-ray source voltage of 40 kV and a source current of 250 μA, without the use of an X-ray filter. Scans were acquired with a voxel

https://doi.org/10.5194/egusphere-2026-1
Preprint. Discussion started: 11 February 2026

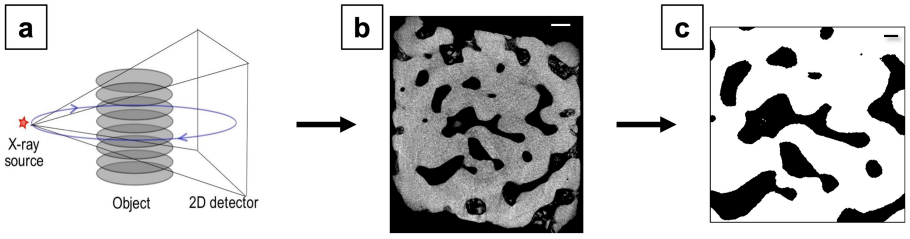

Figure 2. (a) A schematic of the positioning of the x-ray source, object (sample), and x-ray detectors within the micro-CT. (b) An example 2-D grayscale image produced by the micro-CT. (c) An example of a binarized version of the image in (b).

resolution of 15 μm, over a 180°rotation range with a rotation step of 0.7°, and a frame averaging of 5, resulting in scan durations of approximately 30 minutes.

Projection images were reconstructed using the NRecon software into a stack of approximately 900 2-D grayscale slices representing the 3-D structure of the sample. Each slice consists of 1280×1280 pixels, corresponding to an area of 20×20 mm. The reconstructed image stacks were imported into the CTAn software, where a rectangular volume of interest (VOI) measuring $8 \times 8 \times 10$ mm was selected within the sample boundaries. The VOI was positioned to exclude surface defects introduced during sample extraction and cutting.

All subsequent image post-processing was performed using CTAn. This included the application of a 5-pixel Gaussian filter, binarization, and removal of isolated objects smaller than 3x3 pixels (despeckling). In this study, we focus exclusively on the impact of the binarization step; all other acquisition, reconstruction, and post-processing parameters were held constant across samples. While each image processing step has the potential to impact the reconstructed representation of the microstructure of interest, we focus here on the effect of the thresholding step because it is predominantly the first step in micro-CT image processing.

2.2.2 Microstructural Parameters

Micro-CT analysis software and common image-processing toolboxes provide a wide range of parameters for quantifying the microstructure of scanned samples. In this study, we focused on commonly used parameters that describe bulk volume-fraction properties and microstructural complexity. Those parameters include the Percent Object Volume (OV, used to calculate density), Percent Open Porosity (OP), Surface-Area-to-Volume Ratio (S/V), Structural Model Index (SMI), Surface Convexity (SC), and Euler Number (EN). In all analyses, white pixels representing ice were treated as the object, and black pixels were treated as pore space.

The OV (%) is defined as the fraction of the analyzed volume of interest (VOI) occupied by ice. The OP (%) is defined as the fraction of the VOI occupied by pore space that is connected to pore space outside the object. The S/V ($mm^{-}1$) is

https://doi.org/10.5194/egusphere-2026-1
Preprint. Discussion started: 11 February 2026

defined as the ratio of the surface area of the ice matrix to its volume within the VOI, whose reciprocal provides a measure of characteristic structural thickness.

The SMI quantifies the average convexity of the ice matrix surface and provides an indication of the dominant microstructural shape. SMI values of 0, 3, and 4 correspond to ideal plate-, cylinder-, and sphere-like geometries, respectively, while negative values indicate concave surfaces or cavities within the solid matrix. The SMI is calculated by dilating the $3-D$ voxel model and comparing the object surface area before and after dilation, according to:

$$SMI = 6(S'V)/S^2 \tag{1}$$

where S is the object surface area before dilation, S' is the change in surface area due to the dilation, and V is the initial object volume (Hildebrand and Rüegsegger (1997)).

The SC ($mm^{-}1$), also referred to as the fragmentation index, quantifies the relative convexity or concavity of the ice surface by comparing changes in surface area and volume before and after a single-voxel dilation:

$$SC = (S1 - S2)/(V1 - V2) \tag{2}$$

where $S1$ and $S2$ are the object surface areas, and $V1$ and $V2$ are the object volumes, before and after dilation, respectively (Hahn et al. (1992)).

The EN provides a topological measure of the connectedness of the ice matrix and is computed from the three Betti numbers of the three-dimensional solid object:

$$EN = \beta_0 - \beta_1 + \beta_2 \tag{3}$$

where β_0 is the number of connected components, β_1 is the number of tunnels, and β_2 is the number of enclosed cavities.

All microstructural parameters were calculated for the same VOI at each possible binarization threshold value $(0 - 255)$ for each sample. Each threshold was applied globally to every slice in the stack.

2.3 Thresholding Techniques

One of the primary post-processing steps in micro-CT image analysis is the selection of a threshold value for binarizing grayscale images. Although numerous thresholding techniques have been developed, we focus here on three approaches that are particularly relevant for firn and that represent subjective, statistical, and topological strategies, respectively.

1. **CTAn user-defined threshold**: a subjective threshold selected by the user through visual comparison of the grayscale images and their corresponding binarized representations. The threshold is chosen to preserve expected firn microstructural features while minimizing apparent noise and misclassification. To guide this selection, the grayscale intensity

https://doi.org/10.5194/egusphere-2026-1
Preprint. Discussion started: 11 February 2026

histogram, which typically exhibits bimodal peaks corresponding to ice and pore space, is examined to identify a plausible range of threshold values between the two peaks. The user works with individual 2-D slices, and the binarization threshold value selected is applied globally to all slices in the stack.

2. **Otsu's method**: a widely used, automated thresholding technique in image processing that determines an optimal global threshold by minimizing the intra-class variance, defined as the weighted sum of variances within the foreground and background classes (Otsu (1975)).

3. **Persistence Diagram (PD) threshold**: a thresholding technique (Chung and Day (2018)) derived from the field of topological data analysis (TDA) (see, e.g., Carlsson and Vejdemo-Johansson (2021)), a mathematical framework that quantifies the shape of data by tracking the appearance and disappearance of topological features across a filtered space . In the context of grayscale images, we consider the sublevel filtration defined by sweeping a threshold over intensity values. The zeroth Betti number β_0 counts connected components (i.e., isolated dark regions), while the first Betti number β_1 counts loops (i.e., bright regions enclosed by darker areas). The Euler number, defined as $\beta_0 - \beta_1$, provides a scalar summary of these features.

   As the threshold varies, topological features are born and later disappear; their *persistence* is defined as the range of threshold values over which they exist. Features with long persistence are those that remain present across a broad range of thresholds and are therefore less sensitive to small perturbations in intensity, whereas short-lived features are more sensitive to threshold changes and are often associated with noise or minor intensity fluctuations. The PD thresholding preferentially retains features with higher persistence while suppressing those with short persistence. The resulting binary image exhibits topological quantities, including (β_0, β_1, and consequently the Euler number), that are less sensitive to variations in the chosen threshold.

The threshold values identified by each technique are reported in Table 1. Those thresholds were applied to all slices in the stack for each sample, and the resulting binarized images were used to compute the microstructural parameters described in Section 2.2.2 for each sample.

Sample	CTAn User	Otsu's Method	PD Thresholding
7 m	80	97	111
26 m	89	79	67
70 m	82	74	67

Table 1. Threshold values identified by the CTAn User-defined, Ostu's, and Persistent Diagram (PD) methods from the micro-CT data for each sample.

https://doi.org/10.5194/egusphere-2026-1
Preprint. Discussion started: 11 February 2026

2.4 Intrinsic Permeability Simulations

Intrinsic permeability, k, is a quantitative property of a porous material that is determined by the geometry of the pores within and is, by definition, independent of the viscosity and density of a fluid moving through it (Richards and Moore, 1952). When describing the microstructural properties of firn, or any porous material, intrinsic permeability describes the underlying intricacies—pore connectivity and geometry—that proxies such as density and porosity fail to capture.

To estimate the impact of the binarization threshold choice on the underlying microstructure representation, we computed the intrinsic permeability of each sample at six thresholds within the range of reasonable values (60, 70, 80, 90, 100, 110, and 120). The firn microstructure captured in the micro-CT scans at the different threshold values is used to specify the boundary conditions in computational fluid dynamics (CFD) models such that fluid flowing through the digitally reconstructed, three-dimensional pore space can be numerically modeled. By modeling laminar fluid flow through the firn column, we are able to numerically estimate the intrinsic permeability of the collected firn samples using Darcy's Law:

$$k = -\frac{q\nu}{\nabla P} \tag{4}$$

where k is the estimated intrinsic permeability, ν is the simulated viscosity, ∇P is the pressure gradient across the sample, and q is the specific discharge. In the simulations, the viscosity is set to a value that allows for the most numerically stable simulations as the intrinsic permeability is independent of the fluid viscosity, and the specific discharge is calculated as the average velocity of the fluid through the sample. The pressure gradient is specified using pressure boundary conditions at the inlet and outlet that have a prescribed, constant value; the pressure gradient used to estimate the intrinsic permeability is taken as the prescribed pressure difference divided by the sample length. The side boundaries are set as no-flow boundaries. All simulations conducted as part of this research were performed using Palabos (Latt et al., 2021), an open-source Lattice Boltzmann Method (LBM) framework. Below, we provide a brief overview of the LBM, and how it was applied in this research.

2.4.1 The Lattice Boltzmann Method

Unlike other computational fluid dynamics (CFD) methods, the LBM does not directly solve the macroscopic fluid behavior as described by the Navier Stokes equations. Instead, it solves a discretized version of the continuous Boltzmann equation and, as shown by Chapman and Cowling (1990), arrives at the macroscopic solution of fluid flow when the Mach number is sufficiently small ($Ma^2 << 1$) (Qian and Orszag, 1993). The discretized version of the continuous Boltzmann equation, commonly referred to as the Lattice Boltzmann Equation (LBE), is discretized in time, physical space, and velocity space:

$$f_i(\boldsymbol{x} + \boldsymbol{c}_i\Delta t, t + \Delta t) - f_i(\boldsymbol{x}, t) = \Omega_i(\boldsymbol{x}, t) \tag{5}$$

where f_i are particle populations and $\boldsymbol{c}_i$ is a discrete set of velocities that limits the number of directions in which particle populations can advect. As can be seen in Equation 5, the left side of the LBE describes the advection (or *streaming*) of particle populations, and the right side of the LBE describes the collision of particle populations; these two steps are performed in

https://doi.org/10.5194/egusphere-2026-1
Preprint. Discussion started: 11 February 2026

sequence in the LBM. In essence, populations are streamed from location $\boldsymbol{x}$ to locations $\boldsymbol{x} + \boldsymbol{c}_i \Delta t$, after which particles are redistributed between populations due to inter-particle collisions described by the collision operator Ω_i.

In the LBM, the discretization of physical space defines the size of the cells within the global mesh, while the discretization of velocity space defines the discrete set of velocities, $\boldsymbol{c}_i$, with which particles can advect within each cell to reach neighboring cells within the mesh. The choice of velocity space discretization will influence both the scope of simulations that the LBM can accurately model as well as the computational cost. Fewer velocities results in lower computational cost; however, it has been shown that sets with 15 and 19 discrete velocities (D3Q15 and D3Q19) are not rotationally invariant (Silva and Semiao, 2014) and this lack of isotropy can become especially pronounced at high Reynolds numbers when simulating flow through porous media (Suga et al., 2015). Thus, to avoid any potential convergence or accuracy issues with modeling flow through glacial firn microstructure, we employed the 27 velocity set (D3Q27).

2.4.2 Collision Operator in the LBM

Boltzmann's original collision operator considers all possible two-particle collisions for any choice of intermolecular forces (Krüger et al., 2017). However, the collision operators used in the LBM are generally simplified and do not require evaluation of the cumbersome double-integral contained in the original collision operator. When applying the LBM, the collision operator is a modeling choice and should be selected based on the scenario being simulated to ensure numerical results are reliable and free of avoidable error. The simplest and most popular choice for the collision operator is the Bhatnagar-Gross-Krook (BGK) model (Bhatnagar et al., 1954):

$$\Omega_i = -\frac{f_i - f_i^{eq}}{\tau} \tag{6}$$

where τ represents the relaxation time of particle populations toward their equilibrium state, f_i^{eq}. The equilibrium distribution function in its discretized form is (Luo, 1998):

$$f_i^{eq}(\boldsymbol{x}, t) = w_i \rho \left(1 + \frac{\boldsymbol{u} \cdot \boldsymbol{c}_i}{c_s^2} + \frac{(\boldsymbol{u} \cdot \boldsymbol{c}_i)^2}{2c_s^4} + \frac{\boldsymbol{u} \cdot \boldsymbol{u}}{2c_s^2}\right) \tag{7}$$

where $\boldsymbol{u}$ corresponds to the fluid velocity, ρ is the fluid density and the discrete weights, w_i, are associated with the discrete velocity set $\boldsymbol{c}_i$. When using the D3Q27 lattice, the lattice speed of sound is given by $c_s = 1/\sqrt{3}$.

When applying the BGK collision operator, all hydrodynamic quantities are relaxed toward equilibrium at the same rate, τ. This allows the collision computations to be computed without the need for repeated, computationally expensive matrix multiplication. However, the accuracy and stability of this collision model are directly linked to the choice of kinematic viscosity (Talon et al., 2003, 2012) since, in order to recover the macroscopic Navier-Stokes response, the relaxation rate and kinematic viscosity depend on each other:

$$\nu = c_s^2 \left(\tau - \frac{1}{2}\right) \tag{8}$$

https://doi.org/10.5194/egusphere-2026-1
Preprint. Discussion started: 11 February 2026

This limits the range of physical viscosities that can be simulated using this collision operator. Further, the location of solid boundaries mapped into the fluid domain are a function of the fluid viscosity when using the BGK collision operator (Ginzburg and d'Humieres, 2003). This can be particularly problematic when modeling flow through porous media, since accurately describing describing the available pore space and geometry through which fluid can flow is of fundamental importance for generating reasonable estimates of intrinsic permeability. The viscosity-dependence of boundary locations in the BGK collision operator leads to non-physical viscosity dependence in estimates of the intrinsic permeability of polar firn, or any porous medium—intrinsic permeability is a geometric property of a porous material and has no physical connection to the viscosity of the fluid flowing through it.

These shortcomings introduced by the BGK collision operator can be overcome by using more sophisticated collision operators that allow specific hydrodynamic quantities to be relaxed toward equilibrium at different rates. Multiple relaxation time (MRT) collision operators (d'Humières, 2002) have been developed that are capable of relaxing different hydrodynamic quantities toward equilibrium by first transforming populations to moment space and performing the collisions there, and then transforming back to population space. While these models allow for better stability and accuracy over a broader range of viscosities, they involve computationally expensive matrix multiplication. For example, with a D3Q27 velocity model, a 27 x 27 matrix multiplies the 27 population values in each cell when using an MRT collision operator. Further, the optimal MRT parameter settings have only been obtained through numerical studies (Krüger et al., 2017), which makes the use of MRT collision models for general calculations of intrinsic permeability impractical.

A simplification of the MRT collision operator that is still able to overcome the drawbacks of the BGK model is the two-relaxation time (TRT) collision operator (Ginzburg et al., 2008a). In this model, moments are relaxed toward equilibrium using two separate relaxation times. Khirevich et al. (2015) have shown that the TRT collision model can be as efficient as BGK by avoiding matrix-vector multiplication and leveraging the underlying symmetries of the TRT approach. Most importantly for this research, the TRT collision model eliminates viscosity dependence in the location of where solid boundaries are mapped into the fluid domain (Ginzburg et al., 2008b; Pan et al., 2006) such that accurate estimates of intrinsic permeability may be obtained without non-physical errors associated with the choice of collision operator. Fundamental to the TRT model is the decomposition into symmetric ($\boldsymbol{c}_i$) and antisymmetric (-$\boldsymbol{c}_i = \boldsymbol{c}_{\bar{i}}$) parts. The notation for the symmetric and anti-symmetric populations and equilibrium populations are:

$$\begin{aligned} f_i^+ &= \frac{f_i + f_{\bar{i}}}{2}, \quad f_i^- = \frac{f_i - f_{\bar{i}}}{2} \\ f_i^{eq+} &= \frac{f_i^{eq} + f_{\bar{i}}^{eq}}{2}, \quad f_i^{eq-} = \frac{f_i^{eq} - f_{\bar{i}}^{eq}}{2} \end{aligned} \tag{9}$$

where f_i^+ and f_i^{eq+} are the symmetric parts, and f_i^- and f_i^{eq-} are the antisymmetric parts. The lattice Boltzmann equation for this model is then (Ginzburg, 2012):

$$\begin{aligned} f_i^* &= f_i - \lambda^+ \Delta t \left(f_i^+ - f_i^{eq+}\right) - \lambda^- \Delta t \left(f_i^- - f_i^{eq-}\right) \\ f_i\left(\boldsymbol{x} + \boldsymbol{c}_i \Delta t, t + \Delta t\right) &= f_i^*\left(\boldsymbol{x}, t\right) \end{aligned} \tag{10}$$

https://doi.org/10.5194/egusphere-2026-1
Preprint. Discussion started: 11 February 2026

where λ^+ is the relaxation time for even terms and λ^- is the relaxation time for odd terms. The even relaxation time, λ^+ is related to the kinematic viscosity while the ratio between the odd and even relaxation times can be tuned through the so-called magic number, Λ, to maintain a constant mapping of the solid boundary locations into the fluid domain. Λ is defined as:

$$\Lambda = \left(\frac{1}{\lambda^+ \Delta t} - \frac{1}{2}\right)\left(\frac{1}{\lambda^- \Delta t} - \frac{1}{2}\right) \tag{11}$$

through which a constant ratio between the two relaxation times can be maintained. By enforcing $\Lambda = 3/16$, the solid boundary is mapped exactly in the middle between fluid and solid nodes in the mesh (Ginzburg et al., 2008b). Through this relationship, the value of λ^- is set to enforce the desired magic number based on the kinematic viscosity. Similar to BGK, the macroscopic Navier-Stokes behavior is recovered by relating the kinematic shear viscosity, ν, to the λ^+ relaxation rate:

$$\nu = c_s^2 \left(\frac{1}{\lambda^+} - \frac{1}{2}\right) \tag{12}$$

Thus, by maintaining a magic number of 3/16 while using the TRT collision operator, the computational efficiency of the BGK collision operator is maintained while avoiding BGK's non-physical viscosity dependence in mapping solid boundary locations.

3 Results

3.1 Microstructural Properties

To evaluate the influence of binarization threshold selection on the reconstructed representations of the firn microstructure, we calculated each parameter from the stacks of binarized 2-D images (together representing the 3-D sample) generated at each threshold value in the grayscale range (0-255) for each sample (Keegan et al. (2025). The resulting relationships between microstructural parameters and threshold value provide a direct measure of the sensitivity of each parameter to threshold choice. Across all samples, the parameters exhibited two distinct types of behavior: some remained relatively robust over the range of thresholds returned by the CTAn, Ostu, and PD thresholding methods, while others showed pronounced sensitivity to threshold choice.

We quantified threshold sensitivity using the normalized sensitivity range, computed over the interval bounded by the thresholds reported by the CTAn, Otsu, and PD methods, for each parameter. The normalized sensitivity (S) of the parameters was calculated by

$$S = (A_{max} - A_{min})/A_{median} \tag{13}$$

Where A is the microstructural parameter of interest, and A_{max}, A_{min}, and A_{median} are the maximum, minimum, and median values, respectively, of the parameter computed by the threshold values studied. We consider parameters with sensitivities

https://doi.org/10.5194/egusphere-2026-1
Preprint. Discussion started: 11 February 2026

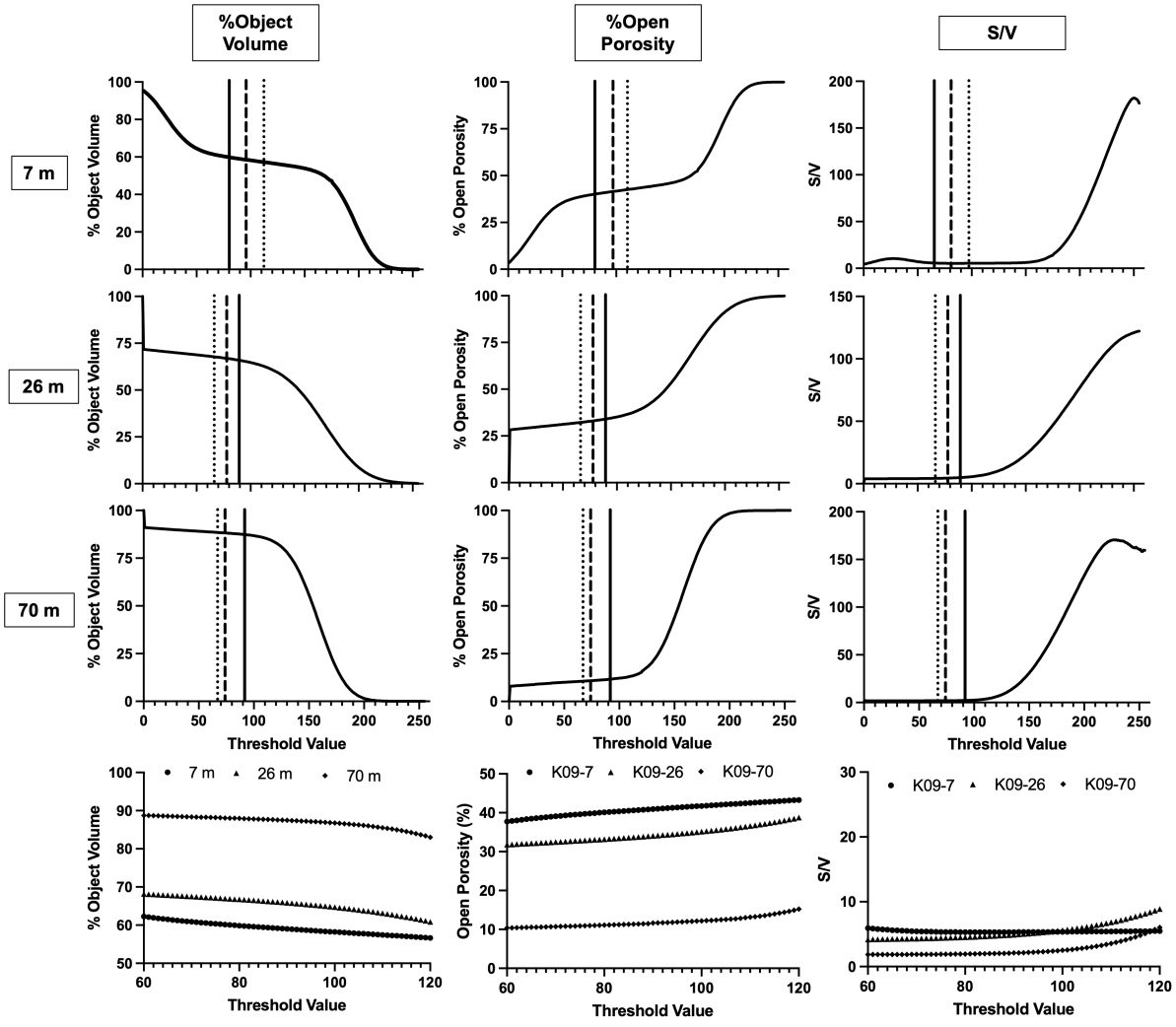

Figure 3. The Percent Object Volume (OV), Percent Open Porosity (OP), and Surface-Area-to-Volume ration (S/V) computed at every possible grayscale threshold value (0-255) for each sample (top three rows), where the solid, dashed, and dotted vertical lines indicate the CTAn, Otsu, and PD method thresholds. The bottom row shows the OV, OP, and S/V calculated over the threshold values of 60-120, a range that would capture the results of nearly all thresholding techniques. Dot, triangle, and diamond markers represent the shallow (7 m), intermediate (26 m), and deep (70 m) firn samples.

of ≤0.05 (≤5% change in the parameter over the range of thresholds) to be robust, 0.05 to 0.20 to be moderately sensitive, and >0.20 to be sensitive to threshold choice.

https://doi.org/10.5194/egusphere-2026-1
Preprint. Discussion started: 11 February 2026

Sample	% Object Volume				% Open Porosity				Surface Area / Volume (mm^-1)			
	CTAn	Otsu	PD	S	CTAn	Otsu	PD	S	CTAn	Otsu	PD	S
7 m	59.1	58.5	57.4	0.03	40.9	41.5	42.6	0.04	5.3	5.4	5.4	0.02
26 m	66.0	66.8	64.5	0.04	34.0	33.1	32.3	0.05	4.9	4.5	4.3	0.13
70 m	87.9	88.2	88.5	0.01	11.2	10.9	10.6	0.05	2.0	1.9	1.9	0.05

Table 2. Robust parameter values calculated at the threshold value identified by the CTAn user-defined (CTAn), Otsu, and Persisent Diagram (PD) thresholding methods from the micro-CT data for each sample, and the normalized sensitivity (*S*) of each.

3.1.1 Robust Mirosctructural Parameters

We first examine the microstructural parameters that exhibit limited sensitivity to binarization threshold choice. The Percent Object Volume (OV), Percent Open Porosity (OP), and Surface-Area-to-Volume ratio (S/V) all display stable behavior across the range of thresholds analyzed (Fig. 3), and therefore we considered these measurements to be robust with respect to threshold selection.

In Figure 3, the OV, OP, and S/V each show a plateau in microstructural parameter values within a range of reasonable thresholds (60-120) in the parameter-threshold value space for each sample. For reference, the threshold values produced by the thresholding techniques considered here are indicated by the vertical solid, dashed, and dotted lines representing the CTAn, Otsu, and PD thresholding techniques, respectively. Across the range of threshold values produced by the three thresholding techniques considered here (Table 1), the sensitivities of OV and OP to threshold were small ($\leq$0.05) for all samples. In the shallow (7 m) and deep (70 m) samples, the S/V was also found to be robust with sensitivities ≤ 0.05, but the intermediate-depth sample was found to be moderately sensitive with a sensitivity of 0.13 (Table 2).

The limited variation observed in these parameters indicates that the bulk volume fractions, are largely insensitive to moderate changes in binarization threshold value determined by common thresholding techniques, for all depths of the firn column. Meanwhile, the S/V, an interfacial length-scale parameter, was also found to be largely insensitive to moderate threshold changes in shallow and deep firn, but moderately sensitive in intermediate-depth firn.

3.1.2 Sensitive Microstructural Parameters

We next examine microstructural parameters that exhibit strong sensitivity to binarization threshold choice. In contrast to bulk-scale parameters, the Structural Model Index (SMI), Surface Convexity (SC), and Euler number (EN) show substantial

https://doi.org/10.5194/egusphere-2026-1
Preprint. Discussion started: 11 February 2026

295 variability across reasonable threshold values (Fig. 4).

Unlike the robust parameters described above, the relationships shown in Figure 4 do not exhibit a plateau near the range of reasonable threshold values (approx. 60-120). Instead, SMI, SC, and EN vary continuously, and in some cases nonlinearly, across the threshold interval defined by the three thresholding techniques (Table 3), resulting in normalized sensitivity values
300 exceeding 0.20 for all but the shallow (7 m) SMI and SC. For the intermediate (26 m) and deep (70 m) firn samples, both SMI and SC are classified as sensitive, while EN exhibits strong sensitivity at all depths (Table 3).

The magnitudes of the sensitivities differ among parameters and with depth. EN displays large variations across the full threshold range for all samples, whereas SMI and SC show more pronounced sensitivity at greater depths. Notably, for the
305 shallow 7-m sample, SC remains relatively insensitive to threshold choice, while SMI exhibits only moderate sensitivity. These results indicate that parameters describing microstructural complexity and connectivity are highly dependent on the threshold selection, particularly for more compact firn, and highlight the importance of threshold selection when interpreting firn microstructural complexity from micro-CT data.

Sample	SMI				Surface Convexity				Euler Number			
	CTAn	Otsu	PD	S	CTAn	Otsu	PD	S	CTAn	Otsu	PD	S
7 m	1.29	1.22	1.24	0.06	1.14	1.09	1.13	0.04	-127	-1176	-1236	0.94
26 m	-7.39	-4.29	-2	1.26	-6	-3.23	-1.42	1.42	20855	11251	4658	1.44
70 m	-11.75	-7.42	-5.75	0.81	-3.85	-2.35	-1.79	0.88	6423	2442	1041	2.2

Table 3. Sensitive parameter values calculated at the threshold value identified by the CTAn user-defined (CTAn), Otsu, and Persisent Diagram (PD) thresholding methods from the micro-CT data for each sample, and the normalized sensitivity (*S*) of each.

3.2 Intrinsic Permeability

310 Threshold value choice impacts the modeled intrinsic permeability, because it changes the reconstructed representation of the sample microstructure. Figure 5 shows that across the threshold range of 60 to 120, the shallow (7 m) and deep (70 m) firn structures exhibit significantly different permeabilities by threshold. Curiously, the permeability of the intermediate-depth (26 m) firn appears relatively insensitive to microstructural changes caused by the changing threshold value (Fig. 5. In repeat laboratory measurements of the permeability of air through firn samples, a measurement error of 5% was found for shallow
315 samples ($\leq 50m$) and 10% for deeper firn samples ($> 50m$;Adolph and Albert (2014)). The error bars included in each panel of Figure 5 represent the estimated 5% error the modeled permeabilities for the shallow (7 m) and intermediate (26 m) samples, and 10% error estimated for the deep (70 m) permeabilities.

https://doi.org/10.5194/egusphere-2026-1
Preprint. Discussion started: 11 February 2026

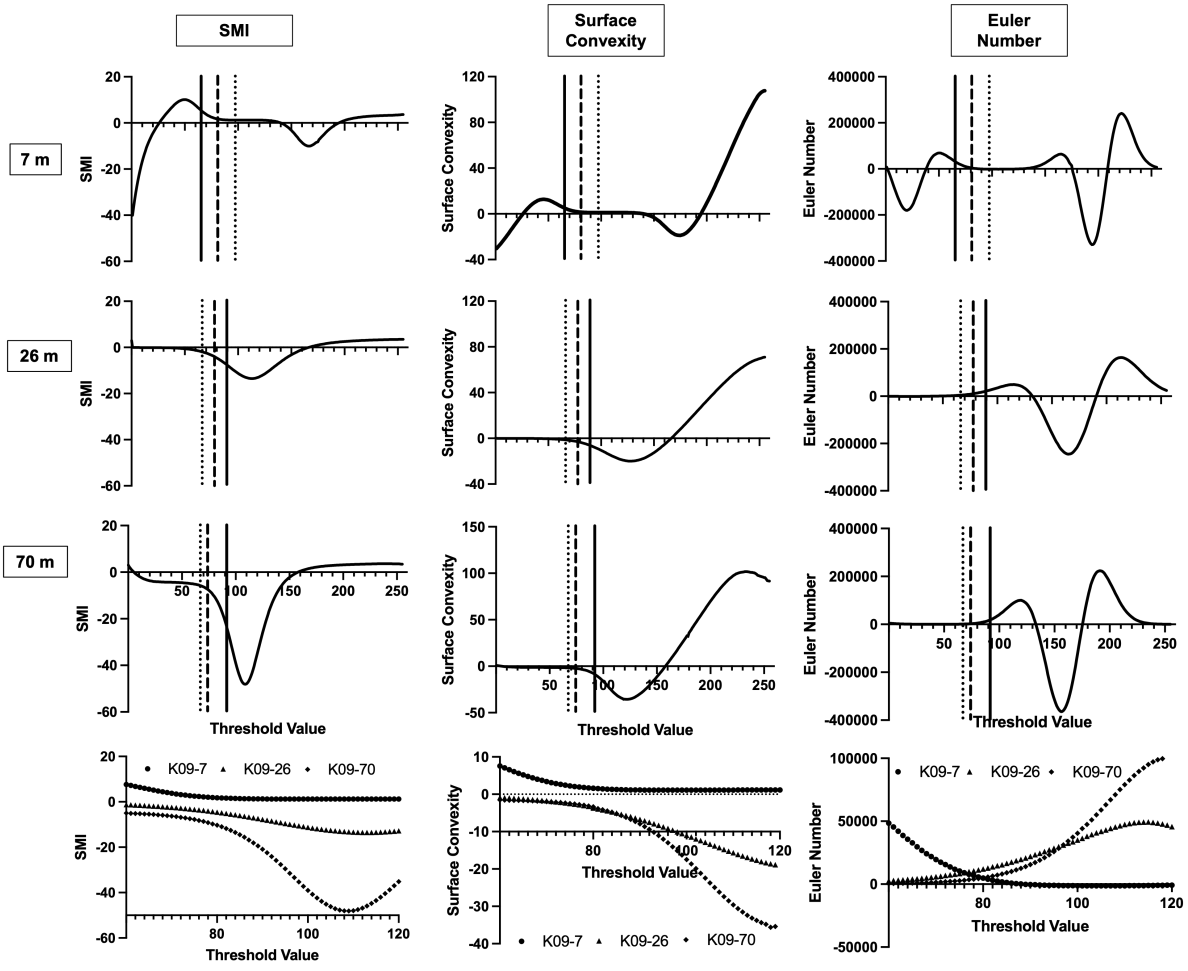

Figure 4. The Structural Model Index (SMI), Surface Convexity (SC), and Euler Number (EN) computed at every possible grayscale threshold value (0-255) for each sample (top three rows), where the solid, dashed, and dotted vertical lines indicate the CTAn, Otsu, and PD method thresholds. The bottom row shows the SMI, SC, and EN calculated over the threshold values of 60-120, a range that would capture the results of nearly all thresholding techniques. Dot, triangle, and diamond markers represent the shallow (7 m), intermediate (26 m), and deep (70 m) firn samples.

4 Discussion

Our results demonstrate that the sensitivity of firn microstructural parameters computed from micro-CT data to binarization threshold choice depend strongly on the type of parameter considered and the firn sample depth. While bulk volume-fraction parameters such as Percent Object Volume (OV) and Percent Open Porosity (OP) remain largely robust across a range of reasonable threshold values, parameters that describe microstructural complexity and connectivity show pronounced and depth-

https://doi.org/10.5194/egusphere-2026-1
Preprint. Discussion started: 11 February 2026

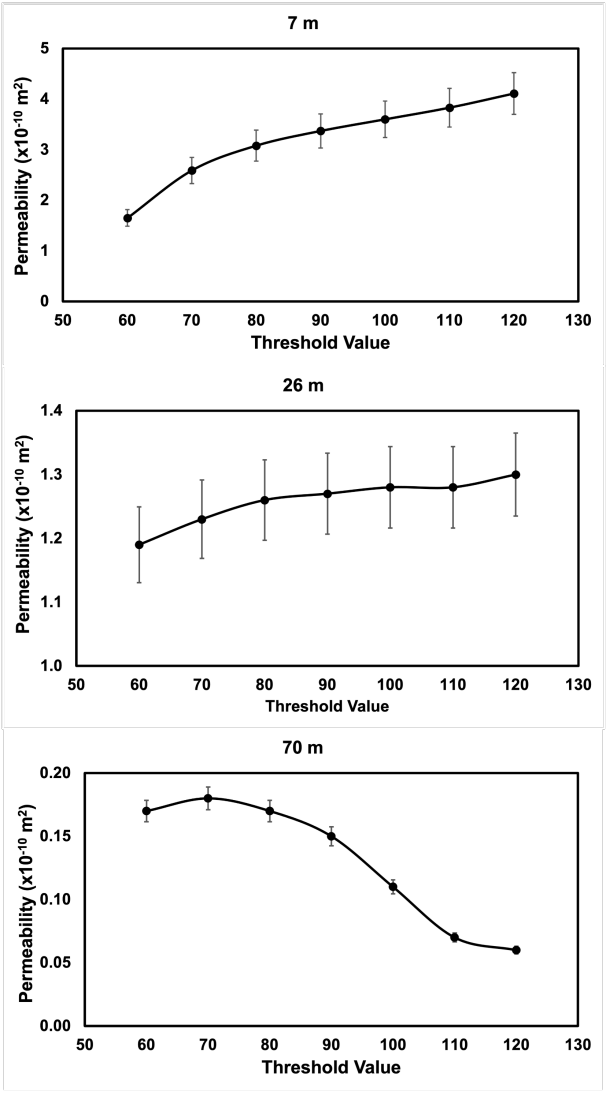

Figure 5. The modeled intrinsic permeability values for the shallow (top panel), intermediate (middle panel), and deep (bottom panel) firn samples over the 60-120 threshold range. Error bars indicate the 5% error for firn $\leq 50m$ and 10% error for firn from $> 50m$ found from laboratory measurementes (Adolph and Albert (2014)).

dependent sensitivity. These results have important implications for the interpretation of firn micro-CT studies, particularly those that seek to infer the geometry, connectivity, or transport-related properties from binarized images.

4.1 Threshold Impact on Microstructure

The observed sensitivity of firn microstructural parameters to the binarization threshold choice results from how the threshold selection alters the representation of the ice-pore interface and the connectivity of small-scale features. Small shifts in the

https://doi.org/10.5194/egusphere-2026-1
Preprint. Discussion started: 11 February 2026

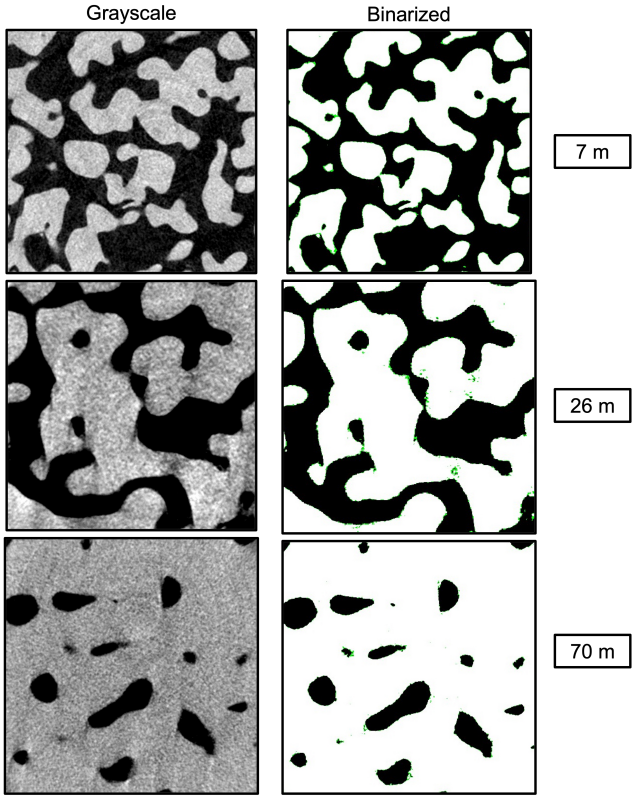

Figure 6. Left: an example grayscale image from the shallow (top), intermediate (middle), and deep (bottom) firn samples. Right: the corresponding binarized images for each sample with the differences in the binarized microstructure between the maximum and minimum thresholds highlighted by green pixels.

threshold can change whether narrow pore throats, thin ice necks, and low-contrast structures are classified as ice or pore space. These variations in binarzied structure can lead to substantial differences in the topology, or microstructural complexity, even when the bulk volume fractions remain largely the same.

Figure 6 highlights the differences in microstructure resulting from the range of threshold values we studied. For each sample, the differences in white pixels (ice-space) generated between the maximum and minimum threshold values are shown as green pixels on the right side of Figure 6. These green pixels are concentrated along the ice-pore interfaces of the images in thin layers that do not substantially change the estimated bulk-volume parameters, such as OV and OP. Calculating the firn densities from the OV further underscores this point as the differences in density computed between the minimum and the maximum threshold for each sample is less than the laboratory measurement error (Appendix A).

Conversely, the concentration of green pixels along the ice-pore interfaces helps explain the strong sensitivity of the SMI, SC, EN, and the intrinsic permeability estimates for these samples. Both the shallow (7 m) and intermediate-depth (26 m) firn samples exhibit multiple narrow neck regions that are fully filled by green pixels in Figure 6, indicating that the higher

https://doi.org/10.5194/egusphere-2026-1
Preprint. Discussion started: 11 February 2026

threshold values reconstruct these features as ice (white pixels). When such narrow pore channels are instead classified as fully connected ice bridges between grains, the geometry and topology of both the pore space and the ice matrix are altered. As a result, not only do estimates of microstructural complexity change, but the connectivity and availability of open pore space for airflow are also reduced, leading to corresponding changes in intrinsic permeability. Figures A1, A2, and A3 in the Appendix further illustrate these microstructural differences in the binarized images.

4.2 Sensitivity Differences by firn zone

Our results show a depth-dependency of the sensitivity of the parameters describing microstructural complexity and connectivity. The S/V, SMI, SC, and EN all display the largest parameter sensitivies for the intermediate-depth (26 m) sample. By design, each of the firn samples we studied represents a different zone of the firn column with different underlying microstructures. In shallow firn, there are only loosely bonded ice grains surrounded by larger pore spaces, resulting in nearly equal amounts of ice and pore-space. While in the intermediate firn, the ice grain and the bonds between them have grown as more compaction and sintering has occurred. This produces more narrow pore throats and thin ice bridges, as well as less surface area due to the larger ice grains. In the deeper firn, the density approaches that of glacial ice and the pore spaces become smaller and more constricted.

When the grayscale image has nearly equal portions of the two classes of objects (ice and pore space in our application), thresholding methods such as Otsu's method behave most stably due to a strong bimodal distribution of the grayscale histogram (Otsu (1975)). The parameter sensitivity results for the shallow (7 m) sample are consistent with this idea, as the sample has just over 50% ice volume (Table 2) and the lowest sensitivities to threshold for nearly all parameters (Tables 2 & 3).

At the intermediate depth (26 m), the pore space has consolidated into fewer but larger pores, accompanied by the growth of ice grains, resulting in lower S/V. This microstructural configuration exhibits the most sensitivity to threshold across all parameters, including those describing bulk volume fractions. In this regime, the addition of white pixels along the ice-pore interface at a higher threshold values can connect larger portions of the ice matrix and close off sections of the open pore space. As a result, variations in threshold at intermediate depths can cause the largest changes in parameters describing both bulk properties and microstructural complexity of the underlying microstucture.

In the deep firn, the microstructure is fairly stable as the ice matrix dominates the firn structure. The addition or subtraction of white pixels along the ice-pore interface due to changes in threshold works to change the shape of the pore spaces. At this depth, the pores are smaller and rounder, and changes to the interface can significantly change the shape of these pores. This leads to higher sensitivities of the SMI, SC, and EN for the 70 m sample than the shallow (7 m) sample, but lower sensitivities than the intermediate-depth (26 m) sample because the pore-ice interface of the deep firn microstructure is smaller.

Interestingly, the intermediate-depth (26 m) sample showed the lowest sensitivity of intrinsic permeability to threshold value, with similar permeability estimates across the range of reasonable threshold values. Conversely, both the shallow (7 m) and deep (70 m) firn samples showed significant differences in intrinsic permeability across the threshold range. These results are also likely due to the underlying microstructure of the firn zone in which they were sampled from. In the shallow firn, the larger number of smaller ice grains and pore throats can merge or separate with the addition or subtraction of white pixels at

https://doi.org/10.5194/egusphere-2026-1
Preprint. Discussion started: 11 February 2026

the interface, which would change the pathways for air to flow through the microstructure. In the deep firn, higher threshold values constrict the already small pore spaces, which would significantly decrease the intrinsic permeability, as seen in Figure 5. At the intermediate-depth, the pore spaces are so large that small variations in the ice-pore interface do not significantly impact the intrinsic permeability of the microstructure.

4.3 Potential impact of other post-processing steps

While the work we present here focuses on the impact of binarization threshold on the microstructural parameters computed from micro-CT data, all image processing steps have the potential to impact the reconstructed microstructure. A systematic study of the impact of all image processing steps, such as those for smoothing and denoising, on the resulting reconstructed firn microstructure would help to determine optimal methods for analyzing firn mirco-CT datasets. The results of such a study would improve our abilities to compare previous snow/firn micro-CT work, as well as produce more accurate representations of firn microstructure for use in fluid-transport modeling.

5 Conclusions

In this study, we examined the sensitivity of firn microstructure measurements computed from micro-CT data to binarization threshold. Using three firn samples spanning shallow, intermediate, and deep sections of the NEEM firn column, we evaluated three common thresholding approaches and quantified the resulting variability in a suite of bulk, geometric, and topological microstructural parameters.

Our results show a clear distinction between parameters that are robust to threshold selection and those that are highly sensitive. Bulk-scale volume-fraction properties, including Percent Object Volume and Percent Open Porosity, exhibited minimal sensitivity to thershold choice across all firn depths, indicating that density- and porosity-related estimates derived from micro-CT are relatively insensitive to moderate variations in the binarization threshold. In contrast, parameters describing microstructural complexity and connectivity (Structural Model Index, Surface Convexity, and Euler Number) showed pronounced sensitivity to threshold selection, with sensitivity increasing with firn depth. The Euler Number, in particular, was sensitive to threshold choice at all depths, underscoring the strong dependence of connectivity-based parameters on binarization threshold. Modeling results of the intrinsic permeability also indicated that variations in threshold significantly impact the resulting permeability due to changes in the underlying microstructure.

These findings demonstrate that while micro-CT-derived bulk firn measurements are generally robust, interpretations of microstructural complexity, topology, and transport-relevant characteristics can be strongly influenced by threshold choice. Care should be taken in selecting a thresholding method to binarize firn micro-CT data when the goal is to estimate the connectivity and complexity of the microstructure.

https://doi.org/10.5194/egusphere-2026-1
Preprint. Discussion started: 11 February 2026

Data availability. All data used to conduct this study, including the microstructural parameters computed for each sample at each possible threshold value and the modeled intrinsic permeabilities at 60, 70, 80, 90, 100, 110, and 120 threshold values, can be found the NSF Arctic Data Center repository: https://arcticdata.io/catalog/view/urn:uuid:877e213e-fb72-463a-b5b8-7a5ee0fc1a65

Author contributions. KK conducted sampling and generated the micro-CT datasets; KK, SD, Y-MC, and MG analyzed the datasets and wrote the manuscript draft.

Competing interests. The authors declare that they have no conflict of interest.

Acknowledgements. This work was supported by the U.S. National Science Foundation Office of Polar Programs Grant 2024163 and the U.S. Army Research Office (ARO) Award W911NF2010131. This work was initiated while Yu-Min Chung was employed at the University of North Carolina at Greensboro.

https://doi.org/10.5194/egusphere-2026-1
Preprint. Discussion started: 11 February 2026

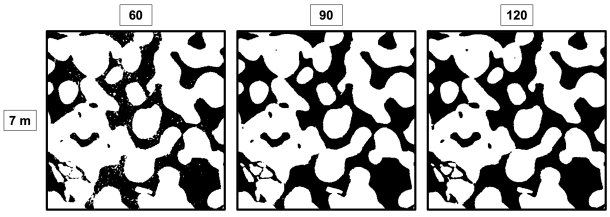

Figure A1. Demonstration of the impact of binarization on the microstructural representation of the shallow (7 m) sample at the 60, 90, and 120 threshold values. White pixels represent ice and black pixels represent pore space.

Appendix A

https://doi.org/10.5194/egusphere-2026-1
Preprint. Discussion started: 11 February 2026

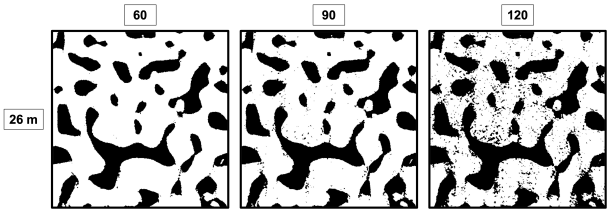

Figure A2. Demonstration of the impact of binarization on the microstructural representation of the intermediate (26 m) sample at the 60, 90, and 120 threshold values. White pixels represent ice and black pixels represent pore space.

https://doi.org/10.5194/egusphere-2026-1
Preprint. Discussion started: 11 February 2026

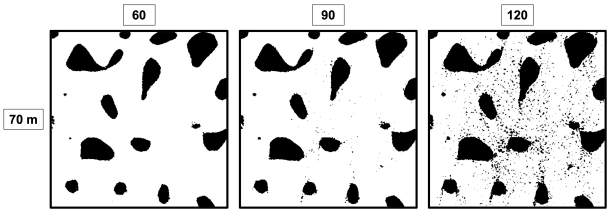

Figure A3. Demonstration of the impact of binarization on the microstructural representation of the deep (70 m) sample at the 60, 90, and 120 threshold values. White pixels represent ice and black pixels represent pore space.

https://doi.org/10.5194/egusphere-2026-1
Preprint. Discussion started: 11 February 2026

References

Adolph, A. C. and Albert, M. R.: Gas diffusivity and permeability through the firn column at Summit, Greenland: measurements and comparison to microstructural properties, The Cryosphere, 8, 319–328, 2014.

Bhatnagar, P. L., Gross, E. P., and Krook, M.: A model for collision processes in gases. I. Small amplitude processes in charged and neutral one-component systems, Physical review, 94, 511, 1954.

Carlsson, G. and Vejdemo-Johansson, M.: Topological Data Analysis with Applications, Cambridge University Press, 2021.

Chapman, S. and Cowling, T. G.: The mathematical theory of non-uniform gases: an account of the kinetic theory of viscosity, thermal conduction and diffusion in gases, Cambridge university press, 1990.

Chung, Y.-M. and Day, S.: Topological Fidelity and Image Thresholding: A Persistent Homology Approach, Journal of Mathematical Imaging and Vision, https://doi.org/10.1007/s10851-018-0802-4, 2018.

Coléou, C., Lesaffre, B., Brzoska, J.-B., Ludwig, W., and Boller, E.: Three-dimensional snow images by X-ray microtomography, Annals of glaciology, 32, 75–81, 2001.

Cuffey, K. M. and Paterson, W. S. B.: The physics of glaciers, Academic Press, 2010.

d'Humières, D.: Multiple–relaxation–time lattice Boltzmann models in three dimensions, Philosophical Transactions of the Royal Society of London. Series A: Mathematical, Physical and Engineering Sciences, 360, 437–451, 2002.

FirnSymposiumTeam: Firn on ice sheets, Nature Reviews Earth & Environment, 5, 79–99, 2024.

Flin, F., Lesaffre, B., Dufour, A., Gillibert, L., Hasan, A., Rolland du Roscoat, S., Cabanes, S., and Pugliese, P.: On the computations of specific surface area and specific grain contact area from snow 3D images, Physics and chemistry of ice, pp. 321–328, 2011.

Forster, R. R., Box, J. E., Van Den Broeke, M. R., Miège, C., Burgess, E. W., Van Angelen, J. H., Lenaerts, J. T., Koenig, L. S., Paden, J., Lewis, C., et al.: Extensive liquid meltwater storage in firn within the Greenland ice sheet, Nature Geoscience, 7, 95–98, 2014.

Freitag, J., Wilhelms, F., and Kipfstuhl, S.: Microstructure-dependent densification of polar firn derived from X-ray microtomography, Journal of Glaciology, 50, 243–250, 2004.

Ginzburg, I.: Truncation errors, exact and heuristic stability analysis of two-relaxation-times lattice Boltzmann schemes for anisotropic advection-diffusion equation, Communications in Computational Physics, 11, 1439–1502, 2012.

Ginzburg, I. and d'Humieres, D.: Multireflection boundary conditions for lattice Boltzmann models, Physical Review E, 68, 066 614, 2003.

Ginzburg, I., Verhaeghe, F., and d'Humieres, D.: Study of simple hydrodynamic solutions with the two-relaxation-times lattice Boltzmann scheme, Communications in computational physics, 3, 519–581, 2008a.

Ginzburg, I., Verhaeghe, F., and d'Humieres, D.: Two-relaxation-time lattice Boltzmann scheme: About parametrization, velocity, pressure and mixed boundary conditions, Communications in computational physics, 3, 427–478, 2008b.

Gow, A. J.: On the rates of growth of grains and crystals in South Polar firn, Journal of Glaciology, 8, 241–252, 1969.

Hagenmuller, P., Chambon, G., Lesaffre, B., Flin, F., and Naaim, M.: Energy-based binary segmentation of snow microtomographic images, Journal of Glaciology, 59, 859–873, 2013.

Hagenmuller, P., Matzl, M., Chambon, G., and Schneebeli, M.: Sensitivity of snow density and specific surface area measured by microtomography to different image processing algorithms, The Cryosphere, 10, 1039–1054, 2016.

Hahn, M., Vogel, M., Pompesius-Kempa, M., and Delling, G.: Trabecular bone pattern factor—a new parameter for simple quantification of bone microarchitecture, Bone, 13, 327–330, 1992.

https://doi.org/10.5194/egusphere-2026-1
Preprint. Discussion started: 11 February 2026

Heggli, M., Köchle, B., Matzl, M., Pinzer, B., Riche, F., Steiner, S., Steinfeld, D., and Schneebeli, M.: Measuring snow in 3-D using X-ray tomography: assessment of visualization techniques, Annals of Glaciology, 52, 231–236, 2011.

Helsen, M. M., Van Den Broeke, M. R., Van De Wal, R. S., Van De Berg, W. J., Van Meijgaard, E., Davis, C. H., Li, Y., and Goodwin, I.: Elevation changes in Antarctica mainly determined by accumulation variability, science, 320, 1626–1629, 2008.

Hildebrand, T. and Rüegsegger, P.: Quantification of bone microarchitecture with the structure model index, Computer Methods in Biomechanics and Bio Medical Engineering, 1, 15–23, 1997.

Hörhold, M. W., Kipfstuhl, S., Wilhelms, F., Freitag, J., and Frenzel, A.: The densification of layered polar firn, Journal of Geophysical Research: Earth Surface, 116, 2011.

Iassonov, P., Gebrenegus, T., and Tuller, M.: Segmentation of X-ray computed tomography images of porous materials: A crucial step for characterization and quantitative analysis of pore structures, Water resources research, 45, 2009.

Kaestner, A., Lehmann, E., and Stampanoni, M.: Imaging and image processing in porous media research, Advances in Water Resources, 31, 1174–1187, 2008.

Keegan, K.: North Greenland Eemian Ice Drilling (NEEM) 2009 S2 Firn Core Density and Permeability, https://doi.org/10.18739/A2SX64931, 2018.

Keegan, K.: Snow metamorphism and firn compaction, 2022.

Keegan, K., Albert, M., and Baker, I.: The impact of ice layers on gas transport through firn at the North Greenland Eemian Ice Drilling (NEEM) site, Greenland, The Cryosphere, 8, 1801–1806, 2014.

Keegan, K., Albert, M., McConnell, J., and Baker, I.: Climate effects on firn permeability are preserved within a firn column, Journal of Geophysical Research: Earth Surface, 124, 830–837, 2019.

Keegan, K., Day, S., and Gardner, M.: NEEM 2009 S2 Firn Core Micro-CT and Intrinsic Permeability Data by Threshold Value, https://arcticdata.io/catalog/view/urn:uuid:877e213e-fb72-463a-b5b8-7a5ee0fc1a65, 2025.

Khirevich, S., Ginzburg, I., and Tallarek, U.: Coarse-and fine-grid numerical behavior of MRT/TRT lattice-Boltzmann schemes in regular and random sphere packings, Journal of Computational Physics, 281, 708–742, 2015.

Krüger, T., Kusumaatmaja, H., Kuzmin, A., Shardt, O., Silva, G., and Viggen, E. M.: The lattice Boltzmann method, Springer International Publishing, 10, 4–15, 2017.

Latt, J., Malaspinas, O., Kontaxakis, D., Parmigiani, A., Lagrava, D., Brogi, F., Belgacem, M. B., Thorimbert, Y., Leclaire, S., Li, S., et al.: Palabos: parallel lattice Boltzmann solver, Computers & Mathematics with Applications, 81, 334–350, 2021.

Lomonaco, R., Albert, M., and Baker, I.: Microstructural evolution of fine-grained layers through the firn column at Summit, Greenland, Journal of Glaciology, 57, 755–762, 2011.

Lundin, J. M., Stevens, C. M., Arthern, R., Buizert, C., Orsi, A., Ligtenberg, S. R., Simonsen, S. B., Cummings, E., Essery, R., Leahy, W., Harris, P., Helsen, M. M., and Waddington, E. D.: Firn Model Intercomparison Experiment (FirnMICE), Journal of Glaciology, 63, 401–422, 2017.

Lundy, C. C., Edens, M. Q., and Brown, R. L.: Measurement of snow density and microstructure using computed tomography, Journal of Glaciology, 48, 312–316, 2002.

Luo, L.-S.: Unified theory of lattice Boltzmann models for nonideal gases, Physical review letters, 81, 1618, 1998.

NEEMCommunityMembers: Eemian interglacial reconstructed from a Greenland folded ice core, Nature, 493, 489–494, 2013.

Otsu, N.: A threshold selection method from gray-level histograms, Automatica, 11, 23–27, 1975.

https://doi.org/10.5194/egusphere-2026-1
Preprint. Discussion started: 11 February 2026

Pan, C., Luo, L.-S., and Miller, C. T.: An evaluation of lattice Boltzmann schemes for porous medium flow simulation, Computers & fluids, 35, 898–909, 2006.

Qian, Y. and Orszag, S.: Lattice BGK models for the Navier-Stokes equation: Nonlinear deviation in compressible regimes, Europhysics letters, 21, 255, 1993.

Richards, L. and Moore, D.: Influence of capillary conductivity and depth of wetting on moisture retention in soil, Eos, Transactions American Geophysical Union, 33, 531–540, 1952.

Schwander, J. and Stauffer, B.: Age difference between polar ice and the air trapped in its bubbles, 1984.

Silva, G. and Semiao, V.: Truncation errors and the rotational invariance of three-dimensional lattice models in the lattice Boltzmann method, Journal of Computational Physics, 269, 259–279, 2014.

Suga, K., Kuwata, Y., Takashima, K., and Chikasue, R.: A D3Q27 multiple-relaxation-time lattice Boltzmann method for turbulent flows, Computers & Mathematics with Applications, 69, 518–529, 2015.

Talon, L., Martin, J., Rakotomalala, N., Salin, D., and Yortsos, Y. C.: Lattice BGK simulations of macrodispersion in heterogeneous porous media, Water resources research, 39, 2003.

Talon, L., Bauer, D., Gland, N., Youssef, S., Auradou, H., and Ginzburg, I.: Assessment of the two relaxation time Lattice-Boltzmann scheme to simulate Stokes flow in porous media, Water Resources Research, 48, 2012.